



HAL
open science

Electron Trapping in Magnetic Mirror Structures at the Edge of Magnetopause Flux Ropes

S. L. Robertson, J. P. Eastwood, J. E. Stawarz, H. Hietala, T. D. Phan, B. Lavraud, J. L. Burch, B. Giles, D. J. Gershman, R. Torbert, et al.

► **To cite this version:**

S. L. Robertson, J. P. Eastwood, J. E. Stawarz, H. Hietala, T. D. Phan, et al.. Electron Trapping in Magnetic Mirror Structures at the Edge of Magnetopause Flux Ropes. *Journal of Geophysical Research Space Physics*, 2021, 126, 10.1029/2021JA029182 . insu-03672443

HAL Id: insu-03672443

<https://insu.hal.science/insu-03672443>

Submitted on 19 May 2022

HAL is a multi-disciplinary open access archive for the deposit and dissemination of scientific research documents, whether they are published or not. The documents may come from teaching and research institutions in France or abroad, or from public or private research centers.

L'archive ouverte pluridisciplinaire **HAL**, est destinée au dépôt et à la diffusion de documents scientifiques de niveau recherche, publiés ou non, émanant des établissements d'enseignement et de recherche français ou étrangers, des laboratoires publics ou privés.



Distributed under a Creative Commons Attribution 4.0 International License

JGR Space Physics



RESEARCH ARTICLE

10.1029/2021JA029182

Electron Trapping in Magnetic Mirror Structures at the Edge of Magnetopause Flux Ropes

Key Points:

- Magnetospheric Multiscale observations show magnetic mirror structures on the edge of magnetopause flux ropes
- Mirror structures trap electrons and have extended 3D structure
- Evolution of mirror structures could facilitate particle acceleration

S. L. Robertson¹ , J. P. Eastwood¹ , J. E. Stawarz¹ , H. Hietala¹ , T. D. Phan² ,
 B. Lavraud³ , J. L. Burch⁴ , B. Giles⁵ , D. J. Gershman⁵ , R. Torbert⁶ ,
 P.-A. Lindqvist⁷ , R. E. Ergun⁸ , C. T. Russell⁹ , and R. J. Strangeway⁹ 

¹Space and Atmospheric Physics Group, Blackett Laboratory, Imperial College London, London, UK, ²Space Sciences Laboratory, University of California, Berkeley, Berkeley, CA, USA, ³Institut de Recherche en Astrophysique et Planétologie, CNRS, UPS, CNES, Université de Toulouse, Toulouse, France, ⁴Southwest Research Institute, San Antonio, TX, USA, ⁵NASA, Goddard Space Flight Center, Greenbelt, MD, USA, ⁶University of New Hampshire, Durham, NH, USA, ⁷KTH Royal Institute of Technology, Stockholm, Sweden, ⁸LASP/Department of Astrophysical and Planetary Sciences, University of Colorado, Boulder, CO, USA, ⁹Institute of Geophysics, Earth, Planetary, and Space Sciences, University of California, Los Angeles, Los Angeles, CA, USA

Correspondence to:

S. L. Robertson,
sadie.robertson14@imperial.ac.uk

Citation:

Robertson, S. L., Eastwood, J. P., Stawarz, J. E., Hietala, H., Phan, T. D., Lavraud, B., et al. (2021). Electron trapping in magnetic mirror structures at the edge of magnetopause flux ropes. *Journal of Geophysical Research: Space Physics*, 126, e2021JA029182. <https://doi.org/10.1029/2021JA029182>

Received 26 JAN 2021
 Accepted 26 MAR 2021

Abstract Flux ropes are a proposed site for particle energization during magnetic reconnection, with several mechanisms proposed. Here, Magnetospheric Multiscale mission observations of magnetic mirror structures on the edge of two ion-scale magnetopause flux ropes are presented. Donut-shaped features in the electron pitch angle distributions provide evidence for electron trapping in the structures. Furthermore, both events show trapping with extended 3D structure along the body of the flux rope. Potential formation mechanisms, such as the magnetic mirror instability, are examined and the evolutionary states of the structures are compared. Pressure and force analysis suggest that such structures could provide an important electron acceleration mechanism for magnetopause flux ropes, and for magnetic reconnection more generally.

1. Introduction

Magnetic reconnection is a fundamental plasma physics process observed throughout the solar system. Reconnection alters the magnetic topology of the plasma environment, allowing different regions of otherwise frozen-in plasmas to mix and releasing energy stored in the magnetic field which accelerates and heats particles (Gonzalez & Parker, 2016; Paschmann et al., 2013). In the context of the Earth's magnetosphere, magnetic reconnection occurs in a variety of locations. At the magnetopause, it enables solar wind and magnetospheric plasmas to mix and is the primary driver of magnetospheric dynamics (Borovsky & Valdivia, 2018; Eastwood et al., 2015).

In addition to its role in controlling the magnetic topology of collisionless space plasmas and releasing stored magnetic energy, magnetic reconnection has also been observed to be a source of energetic particles (Oka et al., 2018). This is most evident in the problem of solar flares, where magnetic reconnection is thought to play a key role in the energy release, and a significant fraction of this energy is found in the nonthermal electron population (Lin, 2006). In situ observations in the Earth's magnetosphere have since demonstrated that energetic particles are often observed. Case studies have independently shown the viability of acceleration processes, with observations of accelerated particles in the vicinity of the diffusion region (Chen et al., 2016; Oieroset et al., 2002), in the magnetotail exhaust associated both with magnetic structure such as islands (Chen et al., 2007) and time-variable outflows (Fu et al., 2013), and at the dipolarization front formed at the leading edge of the Earthward directed reconnection jet in the magnetotail (Fu et al., 2011; Khotyaintsev et al., 2011; Liu et al., 2018).

Many mechanisms for particle acceleration during magnetic reconnection, relying on a variety of different physical processes have therefore been developed, such as Fermi, betatron, stochastic, "surfing," bursty reconnection, inductive, island trapping, and mirroring. Many of these energization processes are associated with the complex substructure that is formed in the vicinity of the reconnection site and in its outflows. It has been suggested that electric fields produced during magnetic reconnection and associated magnetic minima could trap and accelerate particles (Egedal et al., 2005; Hoshino, 2005; Lavraud et al., 2016).

© 2021. The Authors.
 This is an open access article under the terms of the [Creative Commons Attribution License](https://creativecommons.org/licenses/by/4.0/), which permits use, distribution and reproduction in any medium, provided the original work is properly cited.

Fu et al. (2011) proposed that a combination of Fermi and betatron acceleration could be responsible for the energetic particles observed in magnetotail reconnection outflow jets. Other mechanisms involve flux ropes, which are helical magnetic field structures commonly observed on the magnetopause and produced during reconnection (Fear et al., 2008; Russell & Elphic, 1978). Chen et al. (2007) presented observations of energetic electrons and magnetic islands produced during reconnection. Drake et al. (2006) proposed an electron acceleration mechanism in which electrons that are trapped on magnetic island field lines are accelerated in a Fermi-like process as the island contracts. Drake et al. (2012) furthers this argument, suggesting multiple such magnetic islands can merge, resulting in an energetic electron spectra which has an E^2 dependence, consistent with plasma observations throughout the heliosphere. The 3D nature of particle acceleration during magnetic reconnection was investigated by Dahlin et al. (2017), who found that the presence of a guide field can increase the energy of electron populations observed.

Each particle acceleration theory makes specific testable predictions about expected spatial location, anisotropy, power law, and time dependence. For example, merging island models predict the thermal electron population is at marginal firehose stability while the energetic electron energy spectra exhibit power-law behavior, and acceleration in magnetic islands is considered more likely when there is a smaller magnetic shear across the current sheet as this is conducive to island formation. Knowledge of how these processes interact is also crucial, since, for example, one mechanism may provide the seed population for another process, but the relative importance of different phenomena is still not well understood.

A common feature of many particle acceleration mechanisms revolves around the need to trap particles for some time in the acceleration region. The recent observations of Zhu et al. (2019) demonstrate that particle reflection can occur against the flux pile up region at the edge of a magnetopause flux rope, energizing the plasma, and suggests the possibility of magnetic mirror structures playing a role in magnetic reconnection particle acceleration. Although Zhu et al. (2019) did not observe particle trapping, the trapping of particles in magnetic mirror structures is commonly observed in space plasmas. Magnetic holes, often observed in the Earth's magnetosheath, are small-scale depressions in the ambient magnetic field strength which form magnetic mirrors that can trap particles, resulting in anticorrelation between magnetic field strength and plasma pressure (Ahmadi et al., 2017; Horbury et al., 2004). Yao et al. (2018) investigated mirror mode structures observed in the magnetosheath and found them to exhibit particle acceleration features consistent with a mirror instability formation mechanism (Southwood & Kivelson, 1993). Kinetic-scale magnetic holes (KSMH) have also been observed and characterized throughout the magnetosphere (Gershman et al., 2016; Goodrich et al., 2016; Yao et al., 2017). A statistical study of 66 KSMHs in the magnetosheath by Huang et al. (2017) concluded that an electron-vortex formation mechanism to be the most likely candidate and KSMHs have been observed in the vicinity of a magnetopause reconnection site and flux rope (Zhong et al., 2019).

Consequently, the role of magnetic mirror trapping in reconnection dynamics and possible particle acceleration is not yet established. Here we present new Magnetospheric Multiscale (MMS) mission data (Burch et al., 2016) for two case studies of ion-scale flux ropes at the magnetopause, on the edge of which we observe electron trapping in magnetic mirror structures. The mirror structures are found to extend along the body of the flux ropes. In one case study, we observe a second electron trapping feature identified as a KSMH. We discuss the possible formation mechanisms of the magnetic mirrors, as well as how the structures could evolve and produce particle acceleration.

The manuscript is organized as follows. Sections 2 and 3 present observations of the two case studies, observed on January 2, 2017 and December 9, 2015, respectively. Section 4 further discusses the observations, examining instabilities, pressure and force balance, and considering other acceleration mechanisms. Our conclusions are then presented in Section 5.

2. Case Study 1–January 2, 2017

Figure 1 presents 1 hour of survey-mode observations from MMS 2 of a magnetopause crossing on January 2, 2017. During this interval, MMS was moving outbound from the magnetosphere into the magnetosheath at $\sim[9.5, -3, 0] R_e$ GSE, and crossed the magnetopause several times. Data from the Flux Gate Magnetometer (FGM) (Russell et al., 2016), the Fast Plasma Investigation (FPI) (Pollock et al., 2016) and the Electric

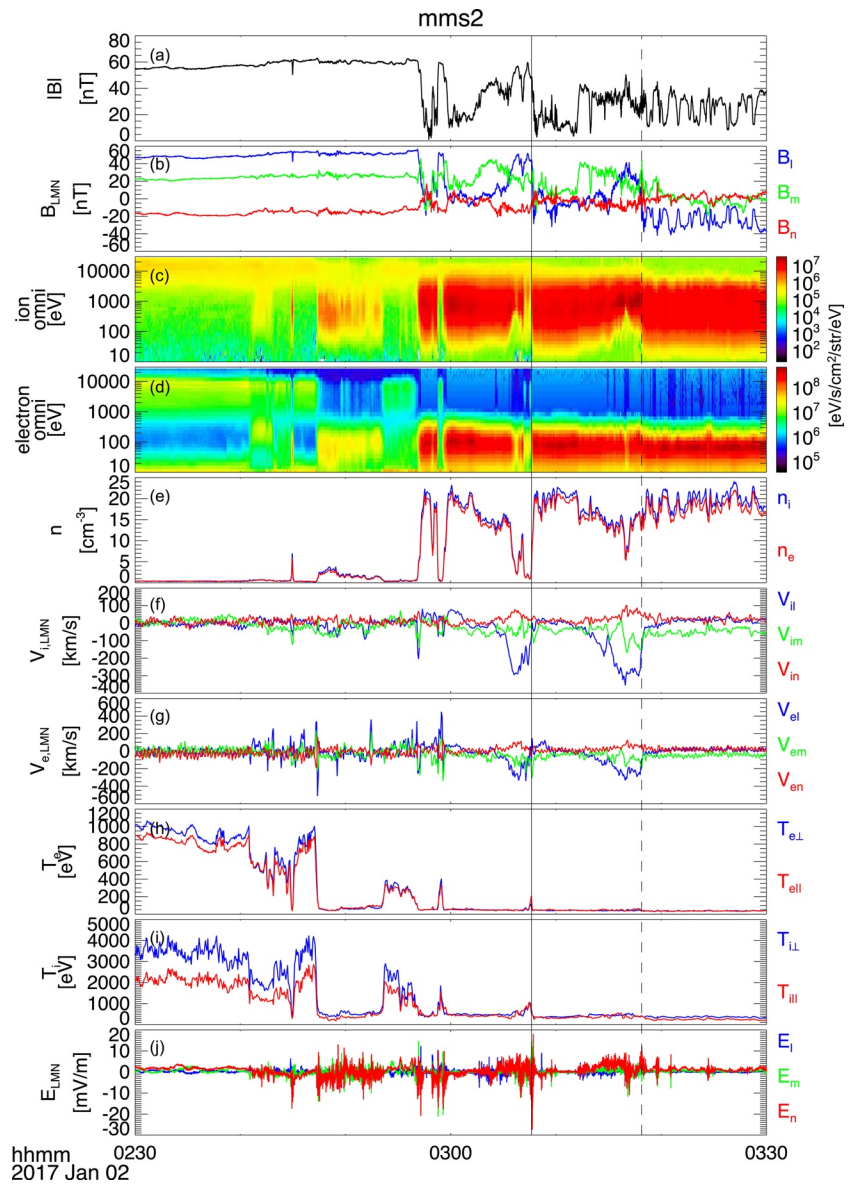


Figure 1. MMS 2 observations of an outbound magnetopause crossing on January 2, 2017. (a and b) magnetic field strength and components in a magnetopause boundary coordinate system (LMN) (c and d) ion and electron omnidirectional energy spectra (e) ion and electron number density (f and g) ion and electron bulk velocity in LMN coordinates (h and i) ion and electron temperature (j) electric field in LMN coordinates. The solid vertical line indicates the magnetopause crossing used to determine the LMN coordinate system and the dashed vertical line indicates the flux rope observation.

Fields instrument (Ergun et al., 2016; Lindqvist et al., 2016) are shown. We note that during this crossing, the data from MMS 3 is incomplete. The data are shown in a magnetopause coordinate system based on minimum variance analysis applied to the complete magnetopause crossing at $\sim 03:07$ UT (marked with a solid vertical line in Figure 1), as this is the cleanest magnetopause crossing closest to the interval of interest. Here $\mathbf{L} = [-0.07, -0.57, 0.82]$ GSE, $\mathbf{M} = [-0.18, 0.80, 0.58]$ GSE, and $\mathbf{N} = [-0.98, 0.19, 0.05]$ GSE. The magnetopause coordinate system is therefore closely aligned with GSE.

During the initial crossings of the magnetopause just prior to 03:00 UT, there is little evidence of a well-developed reconnection exhaust, but at the 03:07 UT encounter, where MMS moved from the magnetosphere (indicated by $+B_L$ oriented magnetic field, low densities, and higher energy particles) to the magnetosheath (indicated by $-B_L$ magnetic field, higher densities and corresponding energy spectra), a reconnection

exhaust was observed in the $-L$ direction ($\sim -z_{\text{GSE}}$ direction). A significant $+B_M$ guide field (~ 20 nT) was observed.

Over the next few minutes between 03:12 and 03:18 UT, a decrease in density, a reversal in B_L to positive values, and an increasing low-energy cut off in the ion energy spectrum was observed. This occurred in conjunction with observations of the reconnection exhaust, and so we identify this interval as a re-encounter of the magnetopause from the magnetosheath side caused by the magnetopause moving Sunwards. During this magnetopause encounter, a flux rope was observed at 03:18 UT, just prior to MMS exiting from the exhaust into the magnetosheath.

The flux rope observations from MMS 2 are shown in greater detail in Figure 2. The flux rope was initially identified by a peak in the magnetic field strength and a corresponding bipolar signature in the $B_{x,\text{GSE}}$ magnetic field component (\sim normal to the magnetopause), accompanied by a peak in the $B_{y,\text{GSE}}$ component of the magnetic field, confirming a helical flux rope structure (Xiao et al., 2004). In the magnetopause coordinate system, the flux rope is identified by a positive/negative bipolar signature in the magnetopause normal component, B_N , and a corresponding peak in magnetic field strength. The axis of the flux rope is identified as being predominantly in the M direction and therefore extends the structure along the magnetopause forming a flux rope. The sign of the B_L component of the magnetic field indicates whether the spacecraft are on the magnetosheath or magnetospheric side of the magnetopause. At the start of the flux rope encounter $B_L \sim 0$, indicating that MMS was close to the magnetopause field reversal. Through the body of the flux rope, the B_L component is negative, but approaches zero at the end of the flux rope encounter indicating the spacecraft traversed the flux rope on the magnetosheath side and exited closer to the magnetopause current sheet. The normal component to the magnetopause B_N is initially negative, becomes positive in the first part of the flux rope and then reverses sign again. Together with the fact that the overall flow is in the $-L$ direction, this is consistent with a flux rope moving in the same direction as the reconnection outflow, as illustrated in Figure 3.

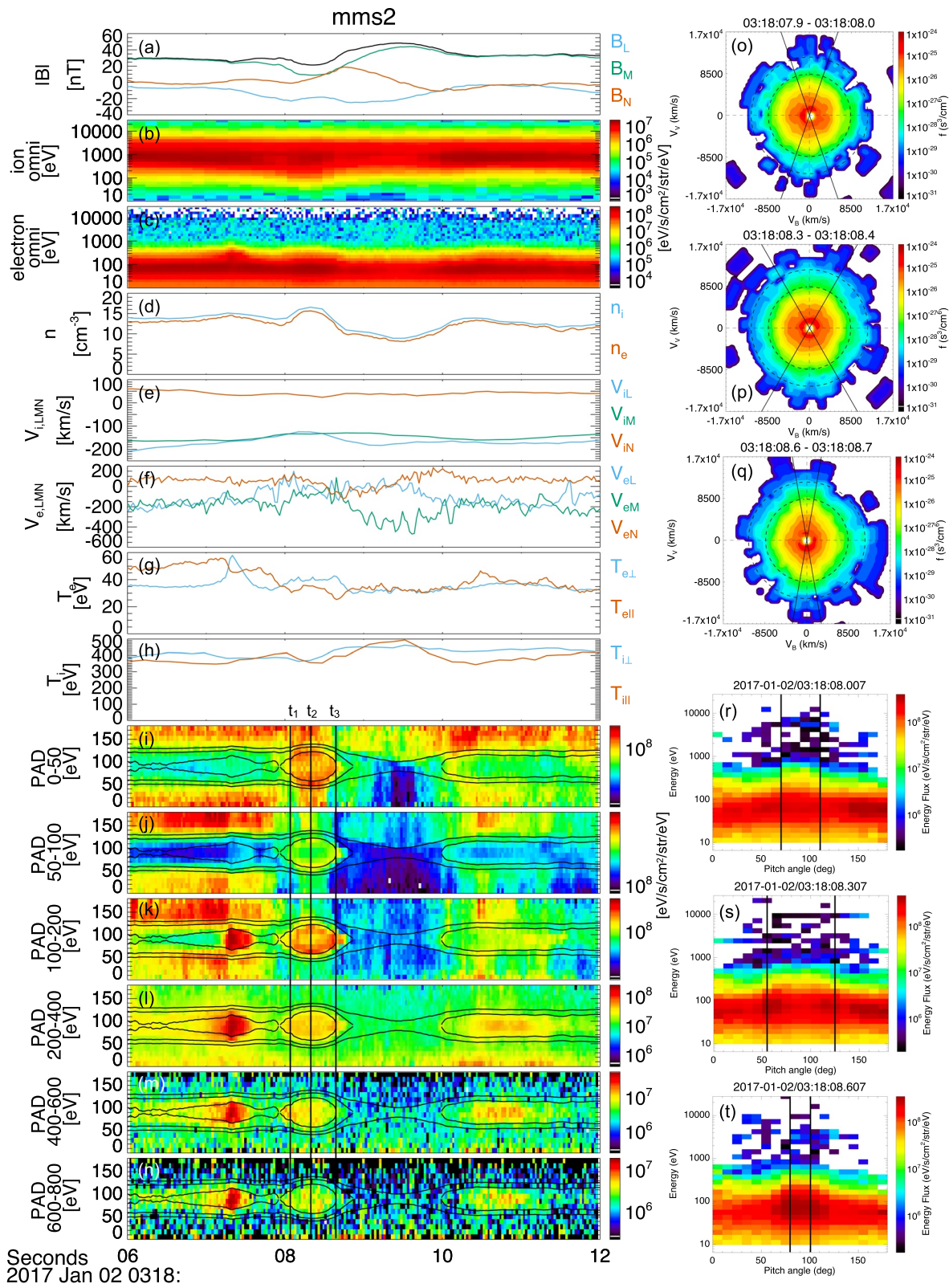
The flux rope observation has a duration of ~ 2.5 s and, based on the average V_{IL} flow speed through the flux rope, the length of the spacecraft path through the flux rope in the GSE L direction is ~ 500 km ($\sim 6.9 d_i$, where $d_i \sim 72$ km is the ion inertial length). This flux rope is therefore comparable in size to the ion-scale flux ropes reported by Eastwood et al. (2016) and Hwang et al. (2018).

Between 03:18:07.9 UT and 03:18:08.7 UT, prior to the spacecraft entering the body of the flux rope, there is a dip in the magnetic field strength of ~ 10 nT. Over this feature, we observe a corresponding peak in the number density of $\sim 5 \text{ cm}^{-3}$ (Figure 2d). An unexpected feature associated with this crater-like structure at the edge of the flux rope is a population of electrons visible in the electron pitch angle distributions, as shown in Figures 2i–2n), where the distributions are split over the energy ranges 0–50, 50–100, 100–200, 200–400, 400–600, and 600–800 eV, respectively. Over-plotted on these distributions are the magnetic mirror loss cone angles for different magnetic mirror strengths (20, 30, and 40 nT). This angle is given by

$$\alpha = \sin^{-1} \sqrt{\frac{B}{B_0}},$$

where B is the observed magnetic field strength and B_0 is the magnetic mirror strength. The increase in energy flux confined by the 20 and 30 nT curves suggests the electrons are trapped within a magnetic mirror with a maximum field strength of ~ 30 nT.

More specifically, at 03:18:07.9 UT, we observe electrons with a dominant perpendicular velocity component which are being reflected at the ~ 30 nT mirror point, corresponding to the peak magnetic field strength observed on the leading edge of the field depression. Figure 2r shows the pitch angle-energy plot at 03:18:08.007 UT where an increase in energy of the electrons at 90° is seen. Figure 2o shows a 2D cut of the 3D electron distribution and we observe a corresponding increase in the radius of the contours in the perpendicular direction. Referring to Figures 2i–2n), the pitch angles of these electrons then spread as the field strength decreases, continuing to be confined by the ~ 30 nT mirror contour until 03:18:08.3 UT where the loss cone angles are $\sim 60^\circ$ and $\sim 120^\circ$. Figure 2s shows the associated increase in energy flux of $\sim 60^\circ$ and $\sim 120^\circ$ electrons in the pitch angle-energy plot. In the energy distribution (Figure 2p), we observe an increase in the radius of the energy contours at $\sim 60^\circ$ and $\sim 120^\circ$ and a flattening at intermediate angles.



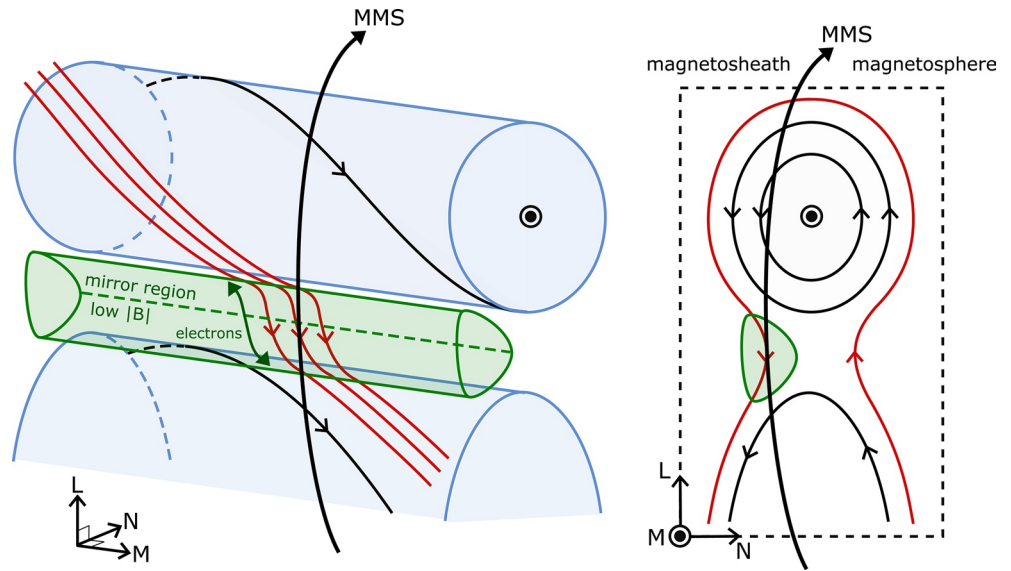


Figure 3. 3-dimensional interpretation for the structure of the flux ropes observed on January 2, 2017 and December 9, 2015.

The pitch angles of the trapped electron populations then converge toward 90° and, at 03:18:08.7 UT, we again observe electrons with a dominant perpendicular velocity component being reflected at the opposing ~ 30 nT mirror point. Figures 2q and 2t show the corresponding pitch angle-energy plot and energy distribution function cut.

The shape of the trapped electron signature in the pitch angle distribution varies over the different energy ranges presented in Figure 2. In Figure 2i, we observe 0–50 eV trapped electrons and electrons with a dominant parallel velocity component, which fill the 30 nT mirror region. In Figure 2k, we observe 50–100 eV electrons forming a very thin donut-shaped feature, as well as a brief period of electrons with a dominant parallel velocity component between 03:18:08.2 UT and 03:18:08.4 UT. In Figure 2k, we observe 100–200 eV electrons forming a thicker donut-shaped feature and have lost the parallel electron signature. In Figures 2l–2n for 200–400, 400–600, and 600–800 eV, respectively, we observe filled-in trapped populations. For energies greater than 800 eV there is no distinguishable trapped electron population.

MMS does not move parallel to the magnetic field over this observation, therefore samples several different flux tubes. Despite this, the continuity of the features described above suggests that the mirror trapped population is coherent and extends along the body of the flux rope, as discussed further below, and we interpret this as a distinct species of mirror-trapped electrons. This is consistent with accepted interpretations in other contexts such as the magnetosheath (e.g., Yao et al., 2018, and references therein). Section 4 presents further discussion of our observations in the context of previous studies. We are therefore able to approximate the dimensions of the structure in both the direction of the spacecraft motion (predominantly in the L component) and along the axis of the flux rope (predominantly the M component). Using the average V_{iL} speed through the trapped population and the ion inertial length calculated for the duration of the flux rope ($d_i \sim 72$ km), we find that the trapped electron population has an observed size of ~ 120 km ($\sim 1.7 d_i$) in the GSE L direction. Throughout the flux rope observation, we also observe a B_M guide field of

Figure 2. MMS 2 observations of a magnetopause flux rope on January 2, 2017 between 03:18:06 UT and 03:18:12 UT. (a) Magnetic field strength and components in a magnetopause boundary coordinate system (LMN) (b and c) ion and electron omnidirectional energy spectra (d) ion and electron number density (e and f) ion and electron bulk velocity in LMN coordinates (g and h) ion and electron temperature (i–n) electron pitch angle distributions over energy ranges 0–50, 50–100, 100–200, 200–400, 400–600, and 600–800 eV, respectively, with over plots of magnetic mirror loss cone angles for 20, 30, and 40 nT magnetic mirrors (o–q) electron energy distributions at times 03:18:07.9–08.0 UT, 03:18:08.3–08.4 UT, 03:18:08.6–08.7 UT, respectively, and approximately corresponding to times t_1 , t_2 , and t_3 , as indicated on pitch angle distribution time series plots. (r–t) Pitch angle energy plots at times 03:18:08.007 UT, 03:18:08.307 UT, 03:18:08.607 UT, respectively, and approximately corresponding to times t_1 , t_2 , and t_3 . Radial lines in plots (o–q) and vertical lines in plots (r–t) show the corresponding mirror loss cone angles.

~ 20 nT. When passing through the mirror-trapped electron populations, we observe a dip in this component of the magnetic field which provides most of the overall magnetic field strength decrease which traps the electrons. The presence of the guide field extends the structure of the mirror-trapped electron population along the body of the flux rope in the M direction. MMS observes two 90° mirror points as it traverses the mirror structure. Based on the orientation of the field in the L - M plane, an estimated lower limit for the extent of the mirror structure in the M direction can be obtained. This is illustrated in Figure 3, where the mirror-trapping magnetic field depression extends along the body of the flux rope. This however assumes that the structure does not significantly evolve over the time of the observations which is reasonable given the duration of the observations. We observe that the average values of the B_M and B_L components are approximately equal over the trapped population, allowing us to geometrically set a minimum value on the M -extent of the trapped population of $\sim 3.4 d_i$.

For completeness, we note that there is a second electron population observed between 03:18:07.2 UT and 03:18:07.5 UT at energies above 100 eV, which exhibits a corresponding $T_{e,perp}$ increase of ~ 20 eV (Figure 2g). This feature is also confined by the 30 nT mirror over plot; however, it is focused to 90° electrons and does not exhibit any donut-like shape (Figures 2i–2m). There is also a slight increase in electron density (Figure 2d). Using the average V_{iL} flow speed through the trapped population and the ion inertial length calculated for the duration of the flux rope ($d_i \sim 72$ km), we find that the trapped electron population has an observed size of ~ 60 km ($\sim 0.8 d_i$) in the GSE L direction. We therefore identify this structure as a kinetic-scale magnetic hole (KSMH) (Huang et al., 2017). Both the KSMH and the mirror trapped electron structure on the edge of the flux rope show evidence of bipolar perpendicular currents over the structures, consistent with electron vortices (e.g., Gershman et al., 2016; Stawarz et al., 2018). These similarities may suggest a relationship between the structures, which could be an interesting area for further investigation.

3. Case Study 2—December 9, 2015

The second case study was observed on December 9, 2015. Figure 4 shows 1 hour of survey-mode observations from MMS 2 for context. During this interval, MMS was again moving outbound from the magnetosphere into the magnetosheath, at $\sim [10, -3.5, -0.5] R_c$ GSE, and crossed the magnetopause multiple times. The data are again shown in a magnetopause coordinate system based on minimum variance analysis applied to the complete magnetopause crossing at 00:51 - 00:54 UT. Here $\mathbf{L} = [0.11, -0.58, 0.80]$ GSE, $\mathbf{M} = [0.42, 0.76, 0.49]$ GSE, and $\mathbf{N} = [-0.90, 0.28, 0.33]$ GSE. After this magnetopause crossing, MMS remained in the magnetosheath until 01:03 UT when the spacecraft crossed the magnetopause and returned to the magnetosphere. During this magnetosheath interval intermittent peaks in V_{iL} , indicate the presence of reconnection exhausts.

Shortly after the magnetopause crossing at 00:51 UT, a flux rope was observed at 00:52:37 UT. The flux rope observations from MMS 2 can be seen in greater detail in Figure 5, where the data is presented in magnetopause LMN coordinates, as in Figure 4. The flux rope was again identified by a peak in the magnetic field strength and a corresponding positive/negative bipolar signature in the B_N component, accompanied by a peak in the B_M component of the magnetic field. The bipolar signature in B_N and large $-V_{iL}$ speed are consistent with a flux rope moving in the same direction as the reconnection outflow. The flux rope observation has a duration of ~ 2.5 s and, based on the average V_{iL} speed through the flux rope, the length of the spacecraft path through the flux rope in the L direction is ~ 563 km $\approx 6.5 d_i$, where $d_i \sim 86$ km, making this an ion-scale flux rope.

Between 00:52:36.7 UT and 00:52:37.4 UT there is a dip in the magnetic field strength of ~ 12 nT and a corresponding peak in the number density of both ions and electrons of ~ 5 cm $^{-3}$ (Figure 4d). Over this period, we also observe donut-like features in the electron pitch angle distributions, signifying mirror-trapped electrons, as discussed in detail in Section 2. The trajectory through the event is very similar to the first event, and so the cartoon in Figure 3 also illustrates the structure of the trapping region in this event. In contrast to the first example, however, throughout this trapped population a significant parallel electron population is observed at the same time as the mirror-trapped electrons.

Using the average V_{iL} speed through the trapped population and ion inertial length calculated for the duration of the flux rope ($d_i \sim 86$ km), we find that the trapped electron population has an observed size

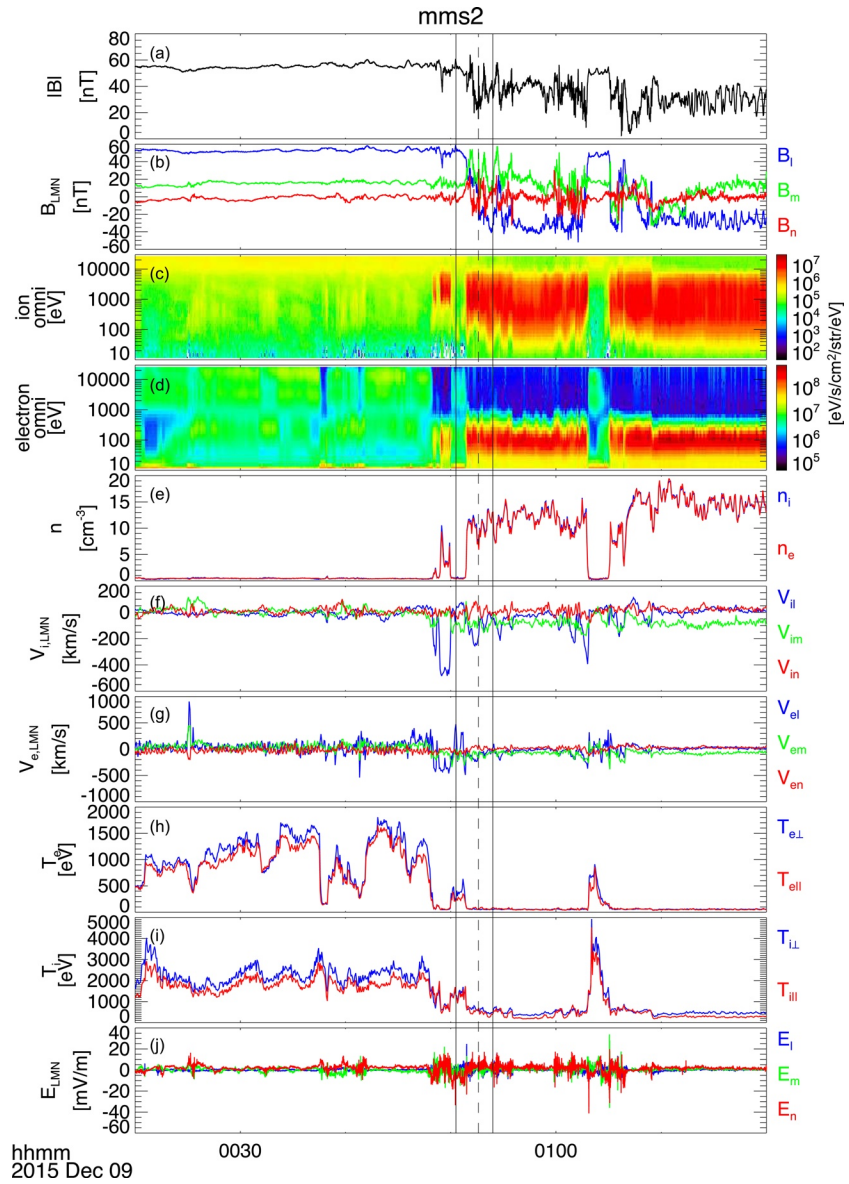


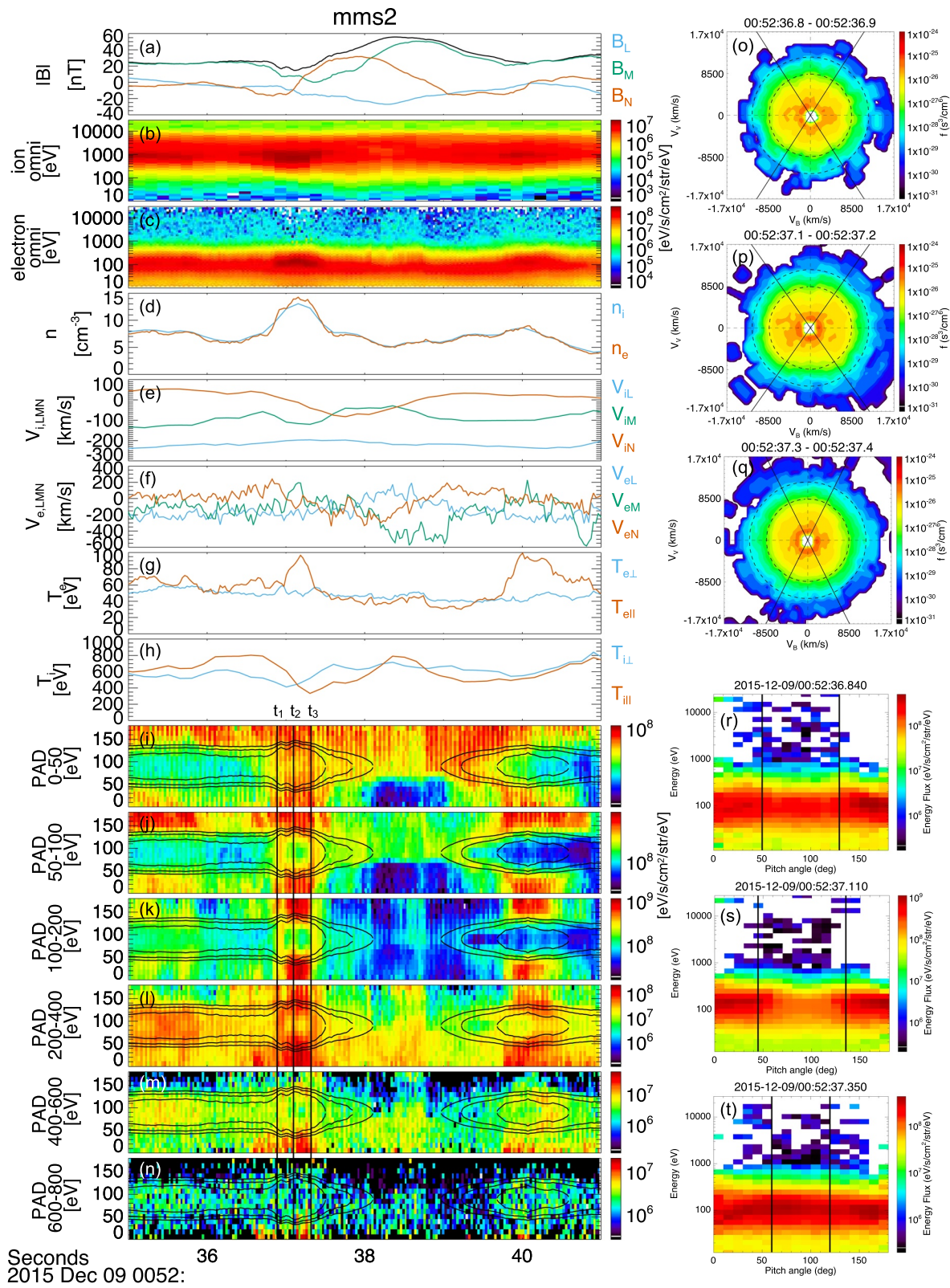
Figure 4. MMS 2 observations of an outbound magnetopause crossing on December 9, 2015. (a and b) magnetic field strength and components in a magnetopause boundary coordinate system (LMN) (c and d) ion and electron omnidirectional energy spectra (e) ion and electron number density (f and g) ion and electron bulk velocity in LMN coordinates (h and i) ion and electron temperature (j) electric field in LMN coordinates. The solid vertical lines indicate the magnetopause crossing used to determine the LMN coordinate system and the dashed vertical line indicates the flux rope observation.

of $\sim 158 \text{ km} \approx 1.8 d_i$ in the L direction. The presence of the guide field also extends the structure of the mirror-trapped electron population into three-dimensions. As detailed in Section 2, we can geometrically set a minimum value on the M -extent of the trapped population of $\sim 3.6 d_i$.

4. Discussion

4.1. Instability Analysis

Magnetic holes with similar donut-shaped pitch angle features have previously been observed in the magnetosheath (Yao et al., 2018) and their formation has been attributed to the ion magnetic mirror instability (Southwood & Kivelson, 1993). The growth of the instability is invoked to explain the characteristic



donut-shaped pitch angle distributions (Kivelson & Southwood, 1996). As the instability grows, the amplitude of the peaks and troughs in the magnetic field strength grow. Electrons trapped between the peaks (in a magnetic mirror of greater magnetic field strength) are Fermi accelerated as the mirror structure grows in amplitude, and their mirror points move closer together. Electrons trapped deeper in the trough (in a magnetic mirror of smaller magnetic field strength) are Fermi decelerated as the trough deepens and the mirror points move further apart. This is shown in the pitch angle distribution as a lower flux of particles at the center of the donut shape and a higher flux at the edges. Furthermore, a betatron acceleration process as the magnetic field strength increases at the peaks, and deceleration as the magnetic field strength decreases in the trough, will enhance this donut-shaped pitch angle feature.

The magnetic mirror instability is driven by a temperature anisotropy with greater perpendicular temperature. In this study, we do not observe significant ion temperature anisotropy. This could suggest that any initial ion temperature anisotropy which could have led to the formation of the mirror-trapped electron populations has since decreased. The trapping region itself is ion-scale, suggesting an instability involving both ions and electrons could play a role in its dynamics (e.g., Kuznetsov et al., 2012). To this extent, we investigate the electron magnetic mirror instability as we do observe a significant temperature anisotropy in the electrons over the trapped population. This instability has a linear theory anisotropy threshold of the form

$$\frac{T_{e\perp}}{T_{e\parallel}} = 1 + \frac{S_e}{\beta_{e\parallel}^{\alpha_e}},$$

where $T_{e\perp}$ and $T_{e\parallel}$ are the perpendicular and parallel electron temperatures, respectively, $\beta_{e\parallel}$ is the parallel electron plasma beta and S_e and α_e are fitting parameters determined by the chosen maximum growth rate of the instability (Gary & Wang, 1996). The whistler anisotropic instability has been shown to follow the same form of linear threshold when $0 \leq \beta_{le} \leq 1000$, however with unique fitting parameters for each given growth rate, $\gamma = \gamma_m / |\Omega_e|$ (the maximum growth rate normalized by the electron cyclotron frequency). The whistler instability has a greater linear growth rate over a wider range of parameters (Gary & Karimabadi, 2006), however recent PIC simulations have suggested that the mirror mode may become dominant after nonlinear saturation (Hellinger & Štverák, 2018).

We also investigate the electron firehose instability, which is similarly driven by a temperature anisotropy, however with greater parallel temperature (Gary & Nishimura, 2003). This instability has a threshold of the form

$$\frac{T_{e\perp}}{T_{e\parallel}} = 1 - \frac{S_e}{\beta_{e\parallel}^{\alpha_e}},$$

where the terms have the same definitions as for the mirror and whistler instabilities.

In Figures 6k and 6v, we plot the electron temperature anisotropy $\frac{T_{e\perp}}{T_{e\parallel}}$ as a function of $\beta_{e\parallel}$ to investigate the proximity of the flux rope observations to these three instability thresholds; such plots are commonly used to investigate plasma stability in the solar wind (e.g., Štverák et al., 2008). The thresholds are plotted as solid line curves and data points for the flux rope observation intervals are color-coded according to observation time. The green curve shows the mirror instability threshold, the red curve shows the whistler instability threshold, and the black curve shows the firehose instability threshold. These thresholds are all for instability growth rates $\gamma = 0.001$, approximating the marginal stability threshold of the instability. This

Figure 5. MMS 2 observations of a magnetopause flux rope on December 9, 2015 between 00:52:35 UT and 00:52:41 UT. (a) magnetic field strength and components in GSE (b and c) ion and electron omnidirectional energy spectra (d) ion and electron number density (e and f) ion and electron bulk velocity in GSE coordinates (g and h) ion and electron temperature (i–n) electron pitch angle distributions over energy ranges 0–50, 50–100, 100–200, 200–400, 400–600, and 600–800 eV, respectively, with over plots of magnetic mirror loss cone angles for 20, 30, and 40 nT magnetic mirrors (o–q) electron energy distributions at times 00:52:36.8–36.9 UT, 00:52:37.1–37.2 UT, 00:52:37.3–37.4 UT, respectively, and approximately corresponding to times t_1 , t_2 , and t_3 , as indicated on pitch angle distribution time series plots. (r–t) Pitch angle energy plots at times 00:52:36.840 UT, 00:52:37.110 UT, 00:52:37.350 UT, respectively, and approximately corresponding to times t_1 , t_2 , and t_3 . Radial lines in plots (o–q) and vertical lines in plots (r–t) show the corresponding mirror loss cone angles.

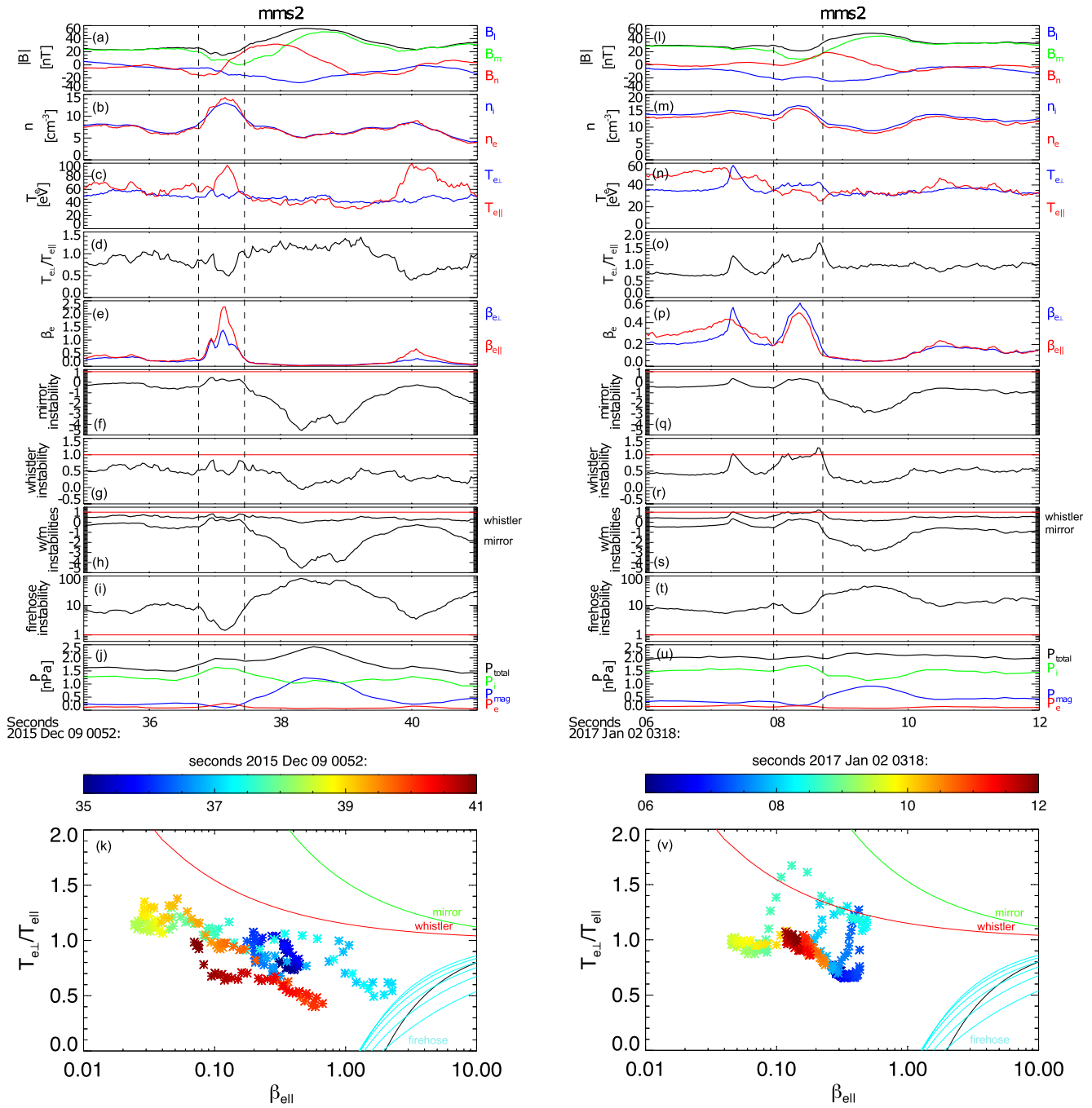


Figure 6. MMS 2 observations of flux ropes observed on December 9, 2015 and January 2, 2017. (a and l) magnetic field components and magnitude in magnetopause coordinate system (LMN), (b and m) ion and electron number density, (c and n) electron parallel and perpendicular temperatures, (d and o) electron temperature anisotropy, (e and p) parallel and perpendicular electron plasma beta, (f and q) electron mirror instability, where threshold is shown by red line (g and r) electron anisotropic whistler instability, where threshold is shown by red line (h and s) combined plots of the electron mirror and anisotropic whistler instabilities (i and t) electron firehose instability, where threshold is shown by red line (j and u) ion, electron, plasma, and total pressure. The dashed vertical lines indicate the electron trapping regions. (k and v) Electron instability analysis scatter plot for corresponding observation windows. The electron mirror instability threshold is shown by the green curve, the anisotropic electron whistler instability threshold is shown by the red curve, and the electron firehose instability threshold is shown by black and blue curves.

corresponds to fitting parameters $S_e = 0.53$ and $\alpha_e = 0.64$ for the mirror instability, $S_e = 0.15$ and $\alpha_e = 0.56$ for the whistler instability (Gary & Karimabadi, 2006), and $S_e = 1.29$ and $\alpha_e = 0.97$ for the firehose instability (Gary & Nishimura, 2003). For the firehose instability, we have also included the other growth rates given in Table 1 of Gary and Nishimura (2003) as shown by the blue curves. In Figures 6f–6i and 6q–6t, we plot this same data as a time series, where the instability thresholds are shown by the red lines. In these plots we have used the $\gamma = 0.001$ threshold for all instabilities.

The observations for both flux ropes exhibit some similarities; as we move through the body of the flux ropes (between ~00:52:37 UT and ~00:52:40 UT for the 2015 case study and between ~03:18:09 UT and 03:18:10.5 UT for the 2017 case study), the electrons tend to move away from both the mirror and firehose instabilities versus the ambient conditions. This can be observed most clearly on the time series plots (Figures 6f, 6i, 6q, and 6t) by the line plots moving away from the red lines which show the instability thresholds. This trend is also potentially observed for the whistler instability (Figures 6g and 6r), however, it is less pronounced. When the mirror-trapped electron populations are observed (between 00:52:36.7 UT and 00:52:37.4 UT for the 2015 case study and between 03:18:07.9 UT and 03:18:08.7 UT for the 2017 case study) the trace for both observations moves toward both the mirror and firehose instabilities, however, to slightly different extents, and we observe differences in the whistler stability. For the 2017 flux rope, we observe that the electrons cross the whistler instability threshold and move toward marginal mirror stability. For the 2015 flux rope, we observe enhancements in the whistler and mirror instability at the edges of the trapped population, where the particles are being reflected at the magnetic mirror point and therefore have high perpendicular velocity, and potentially marginal firehose stability at the center of the trapped population.

The whistler instability observed during the 2017 trapped population suggests the presence of whistler waves, which has been confirmed through wave polarization analysis. Despite not observing the electron mirror instability over the observation, this does not rule out the electron/ion mirror instability as the original formation mechanism of the structure. The instability could have triggered the formation of the structure and any temperature anisotropy may have since diminished. As magnetic mirror modes grow, the temperature anisotropies formed at the center of the structures creates favorable conditions for the formation of whistler waves (Ahmadi et al., 2018), which is consistent with our observations of whistler instability in the 2017 case study.

The 2015 trapped population lies near marginal firehose instability instead of marginal mirror instability, which is likely related to the presence of field aligned electrons on the field lines associated with the mirror structure, which drives up the parallel electron temperature relative to the perpendicular temperature. The presence of field aligned electrons may be attributed to a change in the connectivity of the field (Pu et al., 2013).

The differences in instability observations between the two mirror structures remains an intriguing open question and may represent differences in the ongoing evolution of the two events. For example, the ion mirror instability may be responsible for the initial formation of the mirror structures, with different electron instabilities present over the evolution of the structures. In the 2017 event, a subsequent change in topology of the structure may lead to the presence of the firehose instability. Furthermore, scattering or nonadiabatic deceleration of these field-aligned electrons may lead to their trapping within the mirror structure.

4.2. Pressure and Force Analysis

The above analysis of the formation of the donut-shaped pitch angle distribution discusses the growth of the mirror instability in terms of the wave amplitudes, where the peaks and troughs grow. However, the two observed peaks could also be expanding (contracting) away from (toward) each other, changing the spatial extent of the structure. If the structure were to expand (contract), we would expect to see corresponding Fermi deceleration (acceleration) of the trapped particles. We can investigate the evolution of the structures by examining the pressure profiles and through the use of multispacecraft analysis techniques (see Paschmann & Schwartz, 2000).

Figures 6h and 6q shows the ion, electron, plasma, and total pressures over the flux rope observations. Through the body of both flux ropes, we observe an increase in magnetic pressure and decrease in ion pressure. In the 2017 case study, these changes are approximately balanced (~ 0.7 nPa) and the total pressure remains approximately constant. However, for the 2015 case study, the increase in the plasma pressure (~ 1 nPa) is greater than the decrease in the magnetic pressure (~ 0.3 nPa), resulting in an increase in the total pressure of value of ~ 0.7 nPa.

We also observe differences in the relative pressure profiles for the ions and electrons across the trapped populations in the two case studies. For the 2017 case study, an increase in ion and electron pressures (~ 0.3 and ~ 0.1 nPa, respectively) approximately balances a decrease in magnetic pressure (~ 0.2 nPa), leading to a small increase (~ 0.2 nPa) in total pressure through trapped population (Figure 6h). For the 2015 case study, an increase in electron pressure (~ 0.2 nPa) balances a decrease in magnetic pressure (~ 0.2 nPa) and an increase in ion pressure (~ 0.4 nPa) results in overall pressure enhancement (~ 0.4 nPa) through trapped population (Figure 6q).

For the 2017 case study, any changes in the pressure contributions approximately balance and we observe an approximately constant total pressure. However, in the 2015 case study, we observe imbalances in the pressure contributions and overall pressure enhancements over the trapped population and through the body of the flux rope. The differences in the pressure profiles could indicate different evolutionary states of the phenomena and differences in the roles of the ions and electrons within the two events.

To better understand the structure's dynamics, Figure 7 shows the results of a four-spacecraft force analysis on the 2015 flux rope observations, presented in magnetopause coordinates as determined in Section 3 (note that the absence of data from MMS 3 in the 2017 event precludes the use of this analysis there). The curlometer technique is used to calculate the required gradients and the results are presented at the barycenter of the 4 MMS spacecraft. The ion and electron data are collected at different resolution, therefore the panels containing ion measurements (Figures 7e and 7f) are presented on the ion time-series.

The two vertical lines in Figure 7 at 00:52:36.75 and 00:52:37.45 represent the boundaries of the mirror-trapped electron population. Over the trapped population, we observe signatures in the electron force components. In the $J \times B$ force (Figure 7b) we observe a negative component in the N direction, a positive to negative bipolar signature in the L component and a positive to negative bipolar signature of smaller magnitude in the M component. In the electron pressure gradient force (Figure 7c) we observe enhancements in components through the trapped population with respect to the surrounding plasma, but of a smaller magnitude than the $J \times B$ components. The sum of these two force components can be seen in Figure 7c, where we observe the signatures from the $J \times B$ force to persist. To interpret these electron forces, we refer to Figure 3; the negative force in the N direction is directed away from the magnetic null point and the bipolar L force would act to decrease the L extent of the structure. If the null point was undergoing magnetic reconnection, the force in the $-N$ direction would be overcome by the ram pressure of the inflowing plasma.

Figure 7e shows the ion pressure gradient force where we observe a potential negative-positive bipolar L signature over the trapped population which could be acting to oppose the bipolar force observed in the electron force panels. Figure 7f shows the sum of all force components on the ion time series. Here, we observe no obvious signatures over the trapped population, which would be consistent with the ions acting to balance the electron force components. Furthermore, if the structure has previously contracted, this could show the ion force required to balance the increase in plasma pressure of the collapsed structure. However, the low resolution of the ion measurements means that significance of these observations is unclear. It is also important to note that the observed size of the trapped population ($\sim 1.8 d_i$ in the L direction) means it is an ion-scale structure, suggesting that the gradients we observe are sub-ion scale. Comparison of the measured electric field with the calculated $-\mathbf{v} \times \mathbf{B}$ electric field over this period suggests that the ions are not frozen-in to the magnetic field. Further force analysis is required to determine how the ion dynamics couple into the electron dynamics, specifically through the electric field in the momentum equation, and therefore to determine the precise nature of the dynamics.

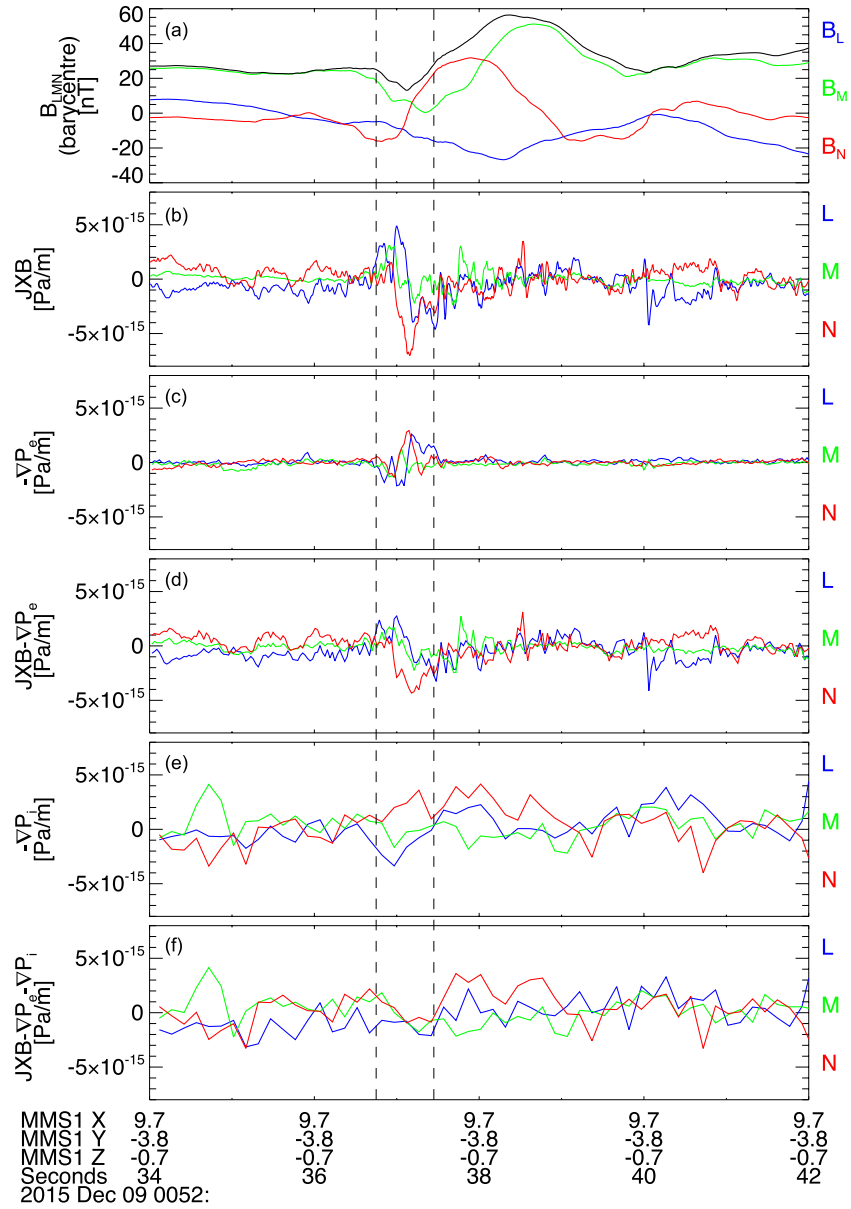


Figure 7. Force analysis of MMS observations of a flux rope observed on December 9, 2015 (a) magnetic field magnitude and components at the MMS spacecraft barycenter in magnetopause coordinates (b) $J \times B$ calculated using the curlometer technique (c) $-\nabla P_e$ (d) $J \times B - \nabla P_e$ (e) ∇P_i (f) $J \times B - \nabla P_e - \nabla P_i$. The dashed vertical lines indicate the electron trapping region.

4.3. Further Acceleration Mechanisms

As discussed in the previous subsections, the potential magnetic mirror instability formation mechanism and the following evolution of the structures facilitates electron acceleration. However, the presence of the flux rope could also play a role in the dynamics of these structures. As well as providing the field enhancement required to trap the particles, the location of the trapped population at the edge of the flux rope near to a null point could produce particle acceleration. If the null point is undergoing magnetic reconnection, the mirror-trapping region would be located in the reconnection inflow region, with the flux rope being located in one of the exhausts. As the electrons trapped in the magnetic mirror structure flow toward the X-point, their mirror points would move closer together as the reconnection inflow converges toward the reconnection site. This converging mirroring of particles would result in a Fermi acceleration process. This

inflow scenario is potentially consistent with the force analysis discussed in Section 4.2, where a Lorentz force is observed in the $-N$ direction, which would be opposed by the ram pressure of the inflowing plasma.

This potential flux rope electron acceleration mechanism invokes the same electron trapping and Fermi acceleration as the Drake et al. (2006) mechanism. However, rather than electron trapping within the body of the flux rope, we have electron trapping in the reconnection inflow region at the edge of the flux rope. This may also impact the magnetic reconnection acceleration mechanism proposed by Egedal et al. (2005) in which electrons are trapped by a parallel electric fields and reconnection-associated magnetic minima.

5. Conclusions

We have shown evidence for electron trapping in magnetic mirror structures on the magnetosheath edge of magnetopause flux ropes. Both case studies have magnetic mirror features consistent with observations of magnetic holes formed via the magnetic mirror instability (e.g., Yao et al., 2018). These magnetic mirror features are located near a magnetic null point next to the flux rope. Both flux ropes have a guide field present which extends the mirror structures along the body of the flux rope.

The results show that magnetic field enhancements associated with flux ropes in magnetic reconnection exhausts can contribute to electron trapping. Unlike other previously proposed trapping mechanisms associated with magnetic islands in which electrons are trapped within the closed (or highly twisted) magnetic topology (Drake et al., 2006), in the structures observed in the present study, the electrons are trapped within magnetic mirrors at the boundary of the flux rope.

Such magnetic mirror structures could prove to be an important feature for particle acceleration at flux ropes and for magnetic reconnection more generally, as they are able to provide the particle trapping required to accelerate particles via Fermi and betatron processes. We have shown that there are electron force signatures present over the trapped populations which could facilitate such acceleration. Further investigation of the evolution of the structures is required to determine the extent of the potential acceleration and to assess the interplay between different energization mechanisms.

Further open questions include how common such structures may be. Here, we identified 2 clear examples from a survey of ~ 90 magnetopause flux ropes. It is important to consider the structures' small size relative to the flux ropes, meaning spacecraft trajectories through the flux ropes and their surroundings are important for encountering the structures. Future studies should plan to investigate such flux rope substructure on statistical scales, addressing how it is influenced by the large-scale dynamics of the reconnection outflows in which it is embedded, and the topology and connectivity of the magnetic field.

Data Availability Statement

Data are publicly available through the MMS Science Data Center (<https://lasp.colorado.edu/mms/sdc/public/>) and were analyzed using the SPEDAS software package for IDL (<http://spedas.org/blog/>).

References

- Ahmadi, N., Germaschewski, K., & Raeder, J. (2017). Simulation of magnetic holes formation in the magnetosheath. *Physics of Plasmas*, 24(12), 122121. <https://doi.org/10.1063/1.5003017>
- Ahmadi, N., Wilder, F. D., Ergun, R. E., Argall, M., Usanova, M. E., Breuillard, H., et al. (2018). Generation of electron whistler waves at the mirror mode magnetic holes: MMS observations and pic simulation. *Journal of Geophysical Research: Space Physics*, 123, 6383–6393. <https://doi.org/10.1029/2018JA025452>
- Borovsky, J. E., & Valdivia, J. A. (2018). The Earth's magnetosphere: a systems science overview and assessment. *Surveys in Geophysics*, 39(5), 817–859. <https://doi.org/10.1007/s10712-018-9487-x>
- Burch, J. L., Moore, T. E., Torbert, R. B., & Giles, B. L. (2016). Magnetospheric multiscale overview and science objectives. *Space Science Review*, 199, 5–21. <https://doi.org/10.1007/s11214-015-0164-9>
- Chen, L.-J., Bhattacharjee, A., Puhl-Quinn, P. A., Yang, H., Bessho, N., Imada, S., et al. (2007). Observation of energetic electrons within magnetic islands. *Nature Physics*, 4, 19. <https://doi.org/10.1038/nphys777>
- Chen, L.-J., Hesse, M., Wang, S., Gershman, D., Ergun, R., Pollock, C., et al. (2016). Electron energization and mixing observed by MMS in the vicinity of an electron diffusion region during magnetopause reconnection. *Geophysical Research Letters*, 43, 6036–6043. <https://doi.org/10.1002/2016GL069215>
- Dahlin, J. T., Drake, J. F., & Swisdak, M. (2017). The role of three-dimensional transport in driving enhanced electron acceleration during magnetic reconnection. *Physics of Plasmas*, 24(9), 092110. <https://doi.org/10.1063/1.4986211>

Acknowledgments

S. L. Robertson was supported by a UKRI/STFC grant ST/S505432/1 and UKRI/NERC grant NE/L002515/1. J. P. Eastwood and J. E. Stawarz were supported by UKRI/STFC grant ST/S000364/1 and J. E. Stawarz is additionally supported by the Royal Society University Research Fellowship URFnR1n201286. The authors thank the MMS team for their work on the mission which was supported by NASA/NSF.

- Drake, J. F., Swisdak, M., Che, H., & Shay, M. A. (2006). Electron acceleration from contracting magnetic islands during reconnection. *Nature*, 443(7111), 553–556. <https://doi.org/10.1038/nature05116>
- Drake, J. F., Swisdak, M., & Fermo, R. (2012). The power-law spectra of energetic particles during multi-island magnetic reconnection. *Acta Pathologica Japonica*, 763(1), L5.
- Eastwood, J. P., Hietala, H., Toth, G., Phan, T. D., & Fujimoto, M. (2015). What controls the structure and dynamics of Earth's magnetosphere? *Space Science Reviews*, 188(1), 251–286. <https://doi.org/10.1007/s11214-014-0050-x>
- Eastwood, J. P., Phan, T. D., Cassak, P. A., Gershman, D. J., Haggerty, C., Malakit, K., et al. (2016). Ion-scale secondary flux ropes generated by magnetopause reconnection as resolved by MMS. *Geophysical Research Letters*, 43, 4716–4724. <https://doi.org/10.1002/2016GL068747>
- Egedal, J., Oieroset, M., Fox, W., & Lin, R. P. (2005). In situ discovery of an electrostatic potential, trapping electrons and mediating fast reconnection in the Earth's magnetotail. *Physical Review Letters*, 94(2), 25006. <https://doi.org/10.1103/PhysRevLett.94.025006>
- Ergun, R. E., Tucker, S., Westfall, J., Goodrich, K. A., Malaspina, D. M., Summers, D., et al. (2016). The axial double probe and fields signal processing for the MMS mission. *Space Science Reviews*, 199(1), 167–188. <https://doi.org/10.1007/s11214-014-0115-x>
- Fear, R. C., Milan, S. E., Fazakerley, A. N., Lucek, E. A., Cowley, S. W. H., & Dandouras, I. (2008). The azimuthal extent of three flux transfer events. *Annales Geophysicae*, 26(8), 2353–2369. <https://doi.org/10.5194/angeo-26-2353-2008>
- Fu, H. S., Khotyaintsev, Y. V., André, M., & Vaivads, A. (2011). Fermi and betatron acceleration of suprathermal electrons behind dipolarization fronts. *Geophysical Research Letters*, 38, L16104. <https://doi.org/10.1029/2011GL048528>
- Fu, H. S., Khotyaintsev, Y. V., Vaivads, A., Retinò, A., & André, M. (2013). Energetic electron acceleration by unsteady magnetic reconnection. *Nature Physics*, 9, 426. <https://doi.org/10.1038/nphys2664>
- Gary, S. P., & Karimabadi, H. (2006). Linear theory of electron temperature anisotropy instabilities: Whistler, mirror, and Weibel. *Journal of Geophysical Research*, 111, A11224. <https://doi.org/10.1029/2006JA011764>
- Gary, S. P., & Nishimura, K. (2003). Resonant electron firehose instability: Particle-in-cell simulations. *Physics of Plasmas*, 10(9), 3571–3576. <https://doi.org/10.1063/1.1590982>
- Gary, S. P., & Wang, J. (1996). Whistler instability: Electron anisotropy upper bound. *Journal of Geophysical Research*, 101(A5), 10749–10754. <https://doi.org/10.1029/96JA00323>
- Gershman, D. J., Dorelli, J. C., Viñas, A. F., Avakov, L. A., Gliese, U., Barrie, A. C., et al. (2016). Electron dynamics in a subproton-gyroscale magnetic hole. *Geophysical Research Letters*, 43, 4112–4118. <https://doi.org/10.1002/2016GL068545>
- Goodrich, K. A., Ergun, R. E., Wilder, F. D., Burch, J., Torbert, R., Khotyaintsev, Y., et al. (2016). MMS Multipoint electric field observations of small-scale magnetic holes. *Geophysical Research Letters*, 43, 5953–5959. <https://doi.org/10.1002/2016GL069157>
- Hellinger, P., & Štverák, Š. (2018). Electron mirror instability: particle-in-cell simulations. *Journal of Plasma Physics*, 84(4), 905840402. <https://doi.org/10.1017/S0022377818000703>
- Horbury, T. S., Lucek, E. A., Balogh, A., Dandouras, I., & Rème, H. (2004). Motion and orientation of magnetic field dips and peaks in the terrestrial magnetosheath. *Journal of Geophysical Research*, 109, A09209. <https://doi.org/10.1029/2003JA010237>
- Hoshino, M. (2005). Electron surfing acceleration in magnetic reconnection. *Journal of Geophysical Research*, 110, A10215. <https://doi.org/10.1029/2005JA011229>
- Huang, S. Y., Du, J. W., Sahraoui, F., Yuan, Z. G., He, J. S., Zhao, J. S., et al. (2017). A statistical study of kinetic-size magnetic holes in turbulent magnetosheath: MMS observations. *Journal of Geophysical Research: Space Physics*, 122, 8577–8588. <https://doi.org/10.1002/2017JA024415>
- Hwang, K.-J., Sibeck, D. G., Burch, J. L., Choi, E., Fear, R. C., Lavraud, B., et al. (2018). Small-scale flux transfer events formed in the reconnection exhaust region between two x lines. *Journal of Geophysical Research: Space Physics*, 123, 8473–8488. <https://doi.org/10.1029/2018JA025611>
- Khotyaintsev, Y. V., Cully, C. M., Vaivads, A., André, M., & Owen, C. J. (2011). Plasma jet braking: Energy dissipation and nonadiabatic electrons. *Physical Review Letters*, 106(16), 165001. <https://doi.org/10.1103/PhysRevLett.106.165001>
- Kivelson, M. G., & Southwood, D. J. (1996). Mirror instability II: The mechanism of nonlinear saturation. *Journal of Geophysical Research*, 101(A8), 17365–17371. <https://doi.org/10.1029/96JA01407>
- Kuznetsov, E. A., Passot, T., & Sulem, P. L. (2012). On the mirror instability in the presence of electron temperature anisotropy. *Physics of Plasmas*, 19(9), 090701. <https://doi.org/10.1063/1.4754008>
- Lavraud, B., Zhang, Y. C., Vernisse, Y., Gershman, D. J., Dorelli, J., Cassak, P. A., et al. (2016). Currents and associated electron scattering and bouncing near the diffusion region at Earth's magnetopause. *Geophysical Research Letters*, 43, 3042–3050. <https://doi.org/10.1002/2016GL068359>
- Lindqvist, P.-A., Olsson, G., Torbert, R. B., King, B., Granoff, M., Rau, D., et al. (2016). The spin-plane double probe electric field instrument for MMS. *Space Science Reviews*, 199(1), 137–165. <https://doi.org/10.1007/s11214-014-0116-9>
- Lin, R. P. (2006). Particle acceleration by the sun: Electrons, hard x-rays/gamma-rays. *Space Science Reviews*, 124(1), 233–248. <https://doi.org/10.1007/s11214-006-9107-9>
- Liu, C. M., Fu, H. S., Vaivads, A., Khotyaintsev, Y. V., Gershman, D. J., Hwang, K. J., et al. (2018). Electron jet detected by MMS at dipolarization front. *Geophysical Research Letters*, 45, 556–564. <https://doi.org/10.1002/2017GL076509>
- Oieroset, M., Lin, R. P., Phan, T. D., Larson, D. E., & Bale, S. D. (2002). Evidence for electron acceleration up to ~300 keV in the magnetic reconnection diffusion region of Earth's magnetotail. *Physical Review Letters*, 89(19), 195001. <https://doi.org/10.1103/PhysRevLett.89.195001>
- Oka, M., Birn, J., Battaglia, M., Chaston, C. C., Hatch, S. M., Livadiotis, G., et al. (2018). Electron Power-law spectra in solar and space plasmas. *Space Science Reviews*, 214(5), 82. <https://doi.org/10.1007/s11214-018-0515-4>
- Paschmann, G., Oieroset, M., & Phan, T. (2013). In-situ observations of reconnection in space. *Space Science Reviews*, 178(2), 385–417. <https://doi.org/10.1007/s11214-012-9957-2>
- Paschmann, G., & Schwartz, S. J. (2000). ISSI book on analysis methods for multi-spacecraft data. In R. A. Harris, (Ed.), *Cluster-II Workshop Multiscale/Multipoint plasma measurements* (Vol. 449, p. 99). Bern, Switzerland: International Space Science Institute. Retrieved from www.issi.unibe.ch
- Pollock, C., Moore, T., Jacques, A., Burch, J., Gliese, U., Saito, Y., et al. (2016). Fast plasma investigation for magnetospheric multiscale. *Space Science Reviews*, 199(1), 331–406. <https://doi.org/10.1007/s11214-016-0245-4>
- Pu, Z. Y., Raeder, J., Zhong, J., Bogdanova, Y. V., Dunlop, M., Xiao, C. J., et al. (2013). Magnetic topologies of an in vivo FTE observed by Double Star/TC-1 at Earth's magnetopause. *Geophysical Research Letters*, 40, 3502–3506. <https://doi.org/10.1002/grl.50714>
- Russell, C. T., Anderson, B. J., Baumjohann, W., Bromund, K. R., Dearborn, D., Fischer, D., et al. (2016). The magnetospheric multiscale magnetometers. *Space Science Reviews*, 199(1), 189–256. <https://doi.org/10.1007/s11214-014-0057-3>

- Russell, C. T., & Elphic, R. C. (1978). Initial ISEE magnetometer results: magnetopause observations. *Space Science Reviews*, 22(6), 681–715. <https://doi.org/10.1007/BF00212619>
- Russell, W., & Parker, E. (2016). Magnetic reconnection. *Astrophysics and Space Science Library*, 427, 10–1007.
- Southwood, D. J., & Kivelson, M. G. (1993). Mirror instability: 1. Physical mechanism of linear instability. *Journal of Geophysical Research*, 98(A6), 9181–9187. <https://doi.org/10.1029/92JA02837>
- Stawarz, J. E., Eastwood, J. P., Genestreti, K. J., Nakamura, R., Ergun, R. E., Burgess, D., et al. (2018). Intense electric fields and electron-scale substructure within magnetotail flux ropes as revealed by the magnetospheric multiscale mission. *Geophysical Research Letters*, 45, 8783–8792. <https://doi.org/10.1029/2018GL079095>
- Štverák, Š., Trávníček, P., Maksimovic, M., Marsch, E., Fazakerley, A. N., & Scime, E. E. (2008). Electron temperature anisotropy constraints in the solar wind. *Journal of Geophysical Research*, 113, A03103. <https://doi.org/10.1029/2007JA012733>
- Xiao, C. J., Pu, Z. Y., Ma, Z. W., Fu, S. Y., Huang, Z. Y., & Zong, Q. G. (2004). Inferring of flux rope orientation with the minimum variance analysis technique. *Journal of Geophysical Research*, 109, A11218. <https://doi.org/10.1029/2004JA010594>
- Yao, S. T., Shi, Q. Q., Liu, J., Yao, Z. H., Guo, R. L., Ahmadi, N., et al. (2018). Electron dynamics in magnetosheath mirror-mode structures. *Journal of Geophysical Research: Space Physics*, 123, 5561–5570. <https://doi.org/10.1029/2018JA025607>
- Yao, S. T., Wang, X. G., Shi, Q. Q., Pitkänen, T., Hamrin, M., Yao, Z. H., et al. (2017). Observations of kinetic-size magnetic holes in the magnetosheath. *Journal of Geophysical Research: Space Physics*, 122, 1990–2000. <https://doi.org/10.1002/2016JA023858>
- Zhong, Z. H., Zhou, M., Huang, S. Y., Tang, R. X., Deng, X. H., Pang, Y., & Chen, H. T. (2019). Observations of a kinetic-scale magnetic hole in a reconnection diffusion region. *Geophysical Research Letters*, 46, 6248–6257. <https://doi.org/10.1029/2019GL082637>
- Zhu, C., Zhang, H., Fu, S., Ni, B., Strangeway, R. J., Giles, B. L., et al. (2019). Trapped and accelerated electrons within a magnetic mirror behind a flux rope on the magnetopause. *Journal of Geophysical Research: Space Physics*, 124, 3993–4008. <https://doi.org/10.1029/2019JA026464>